Spatial Transformation of Motion and Deformation Fields Using Nonrigid Registration

A. Rao*, R. Chandrasekara, G. I. Sanchez-Ortiz, R. Mohiaddin, P. Aljabar, J. V. Hajnal, B. K. Puri, and D. Rueckert

Abstract—In this paper, we present a technique that can be used to transform the motion or deformation fields defined in the coordinate system of one subject into the coordinate system of another subject. Such a transformation accounts for the differences in the coordinate systems of the two subjects due to misalignment and size/shape variation, enabling the motion or deformation of each of the subjects to be directly quantitatively and qualitatively compared. The field transformation is performed by using a nonrigid registration algorithm to determine the intersubject coordinate system mapping from the first subject to the second subject. This fixes the relationship between the coordinate systems of the two subjects, and allows us to recover the deformation/motion vectors of the second subject for each corresponding point in the first subject. Since these vectors are still aligned with the coordinate system of the second subject, the inverse of the intersubject coordinate mapping is required to transform these vectors into the coordinate system of the first subject, and we approximate this inverse using a numerical line integral method. The accuracy of our numerical inversion technique is demonstrated using a synthetic example, after which we present applications of our method to sequences of cardiac and brain images.

Index Terms—Atlas, brain deformation, cardiac motion, conjugate map, diffeomorphism, numerical inverse.

I. INTRODUCTION AND BACKGROUND

VECTOR fields which describe the spatio-temporal characteristics of anatomical structures are frequently used to study biological processes such as motion and growth. Typically, the motion or deformation fields are derived from a series of medical images acquired at different time points. For example, longitudinal neuro-imaging studies which follow individual subjects over several years are frequently used to assess long-term structural changes in the brain due to growth or atrophy. The deformation fields associated with long-term structural changes in the brain can be calculated using techniques such as nonrigid registration [1]–[4]. In cardiac imaging, the spatio-temporal analysis of images acquired over a cardiac cycle can be used to study the motion and deformation of the heart as it contracts. For example, Chandrasekara *et al.* [5] have used nonrigid registration to reconstruct the 4D motion field describing cardiac motion from tagged magnetic resonance imaging (MRI) images [6], [7]. Other authors have proposed algorithms for the reconstruction of myocardial motion by using optical flow techniques [8], [9] or by explicitly tracking tag lines and planes [10]–[17]. In all cases, the resulting vector fields are defined with respect to the coordinate system of the anatomy of the chosen subject at some temporal reference point.

Although any qualitative or quantitative inspection of the vector field derived from any particular subject may allow the assessment of the function of (motion), or changes in (deformation) the subject's anatomy, one cannot directly compare the vector fields from different subjects because of differences in their anatomical coordinate systems. These differences arise from different subject alignment and variations in the size and shape of the subject anatomies. In this paper, we describe a technique which can be used to align and transform the vector field of a particular subject into the coordinate system of another subject (i.e., a *reference* subject), thereby enabling both vector fields to be qualitatively and quantitatively compared in a common coordinate system. The spatial transformation of the vector fields is facilitated by using nonrigid registration to calculate an intersubject mapping between both coordinate systems which is then inverted using a numerical technique and applied to the original motion/deformation field of the first subject. The resulting transformed vector field is then defined in the coordinate system of the second subject.

The motion and deformation fields that we transform in this paper describe external, visible macroscopic properties of a subject's anatomy, which enables us to directly apply intersubject mappings when transforming from one coordinate system to another. To the best of our knowledge, there are no previous publications that address the transformation of such fields. However, spatial transformation schemes have been proposed [18]–[20] that deal with the transformation of MR diffusion images to a single "reference" coordinate system. Such images have a symmetric second-order tensor defined at every voxel that describes the local diffusive behavior of water at the corresponding point in the imaged material. Since the principal diffusivity directions are characterized by the eigenvectors of the diffusion tensor, the proposed transformation schemes seek to preserve the direction of the eigenvectors with respect to subject anatomy. Although these methods are facilitated by calculating a reference-subject mapping using image registration of corresponding MR images, they do not transform the tensor image by

simply applying the reference-subject mapping using a tensor transformation law. This is because the registration of the MR images yields a correspondence between reference and subject that does not hold at microscopic scales. For example, we do not expect a subject with a larger brain than another subject to have larger water molecules even though specific regions within the larger brain may indeed be bigger. Instead we would expect the larger brain to contain more, rather than bigger, water molecules. Since the diffusion tensor describes microscopic cellular properties of a subject, it would be inappropriate to use the mapping derived from the anatomical MR images to transform it into the reference coordinate system. In our paper, we are concentrating on the transformation of motion and deformation fields, each of which are implicitly macroscopic properties since they describe external, observable anatomical changes rather than internal, hidden cellular phenomena. We can, therefore, directly apply intersubject mappings to our motion /deformation fields when transforming them.

In Section II, we describe each of the steps required to perform the spatial transformation, before presenting a validation of the proposed transformation technique using synthetic data in Section III-B. The results obtained using clinically acquired heart and brain data are then given in Sections III-C and III-D, respectively, while Section IV presents some conclusions and directions for future work.

II. METHOD

A. Motion/Deformation Field Derivation

The first step in our process requires the calculation of the deformation pattern/motion fields for a subject S that we will later map into the coordinate system of a second subject R, referred to as the reference subject. Given a sequence of images $S_i, i = 0, \ldots, n$ which show the anatomy for subject S at $n + 1$ different time points, we first have to choose an image within this sequence relative to which the derived deformation/motion field will be expressed. Let this image be S_0 with coordinate system (x', y', z'), and let the corresponding image for R be R_0 with coordinate system (x, y, z). This makes (x, y, z) the reference coordinate system to which we will ultimately map the original motion/deformation fields of subject S. These fields are calculated by using a suitable tracking/nonrigid registration algorithm to give a set of transformations $\mathbf{T}_{(0,i)}^S(x', y', z')$ relating S_0 to every image S_i in the sequence. The actual deformation/motion fields $\mathbf{D}_{(0,i)}^S(x', y', z')$ that we require are then given by

$$\mathbf{D}_{(0,i)}^S(x', y', z') = \mathbf{T}_{(0,i)}^S(x', y', z') - (x', y', z').$$

In principle, any motion or deformation field defined in the coordinate system (x', y', z') can be transformed into the coordinate system of subject R regardless of how it has been calculated. For example, we could transform a synthetically generated field defined in this coordinate system if we so wished. However, the images S_0 and R_0 are still required to determine the intersubject mapping that facilitates the field transformation.

B. Transformation of Deformation/Motion Fields

In order to actually transform the deformation/motion field for S, we need to calculate a mapping between coordinate systems (x', y', z') and (x, y, z). To do this, we can perform a nonrigid registration of image R_0 to S_0 (in this paper we use the

algorithm described in Section III-B). This produces a mapping $\mathbf{F}_{(R,S)}$

$$\mathbf{F}_{(R,S)} : (x, y, z) \longmapsto (x'(x, y, z), y'(x, y, z), z'(x, y, z)).$$

Although any nonrigid registration technique can be used to determine this mapping, we must ensure that the mapping is diffeomorphic, i.e., that it is differentiable and has a differentiable inverse so that our field transformation technique can be used.

Although the aim of our technique is to transform the field vectors $\mathbf{D}_{(0,i)}^S(x', y', z')$ $i = 1, \ldots n$ into the coordinate system of R, in practice we also want the transformed field to be defined on a specific set of R coordinates, eg. the voxel positions of R_0, since this will enable us to directly compare the transformed fields of a number of different subjects. Given such a set of coordinates X, consider a point P with R coordinates $\boldsymbol{x}_0 = (x_0, y_0, z_0) \in X$. The transformed field vector $\tilde{\mathbf{d}}^S$ that will be placed at this location is equal to

$$\tilde{\mathbf{d}}^S = \mathbf{F}_{(R,S)}^{-1}(\boldsymbol{x}_0' + \mathbf{d}^S) - \boldsymbol{x}_0$$

where

$$\boldsymbol{x}_0' = (x_0', y_0', z_0') = \mathbf{F}_{(R,S)}(\boldsymbol{x}_0)$$

are the coordinates of P expressed in the coordinate system of S and $\mathbf{d}^S$ is the original untransformed field vector at $\boldsymbol{x}_0'$. Note that since the original field $\mathbf{D}_{(0,i)}^S(x', y', z')$ may not be explicitly defined at $\boldsymbol{x}_0'$, an interpolation method may be required to determine the untransformed vector $\mathbf{d}^S$. Such an interpolation should be straightforward because $\mathbf{D}_{(0,i)}^S(x', y', z')$ will be defined on a regular grid of S coordinates, i.e., the voxel positions of S_0. Clearly, the transformation requires a calculation of the inverse mapping $\mathbf{F}_{(R,S)}^{-1}$ which, in theory, one could calculate by registering image S_0 to R_0. In practice, however, it is likely that the calculated inverse would be inconsistent with the original mapping, i.e., their composition would not be identity. While image registration techniques exist which ensure the consistency of the original mapping and its inverse [21] we have chosen to use a numerical method to directly determine the inverse from the original mapping. Another possibility that avoids these consistency issues would be to calculate and use just the inverse mapping $\mathbf{F}_{(R,S)}^{-1}$ to transform the field vectors $\mathbf{D}_{(0,i)}^S(x', y', z')$ at a specific set of S coordinates rather than at a specific set of R coordinates, and then use an interpolation method to calculate the transformed field at the required R locations. The drawback of this method is that the required interpolation would be difficult because the uninterpolated transformed field would be defined on a nonuniformly distributed set of R coordinates. Thus, we prefer to calculate the mapping $\mathbf{F}_{(R,S)}$ and approximate its inverse using our numerical technique.

In order to determine $\tilde{\mathbf{d}}^S$, consider a path $\mathcal{L} : \boldsymbol{x}(\theta), \theta \in [0, 1]$ defined in the coordinate system of R that represents the transformed motion or deformation vector, i.e.,

$$\boldsymbol{x}(0) = \boldsymbol{x}_0, \boldsymbol{x}(1) = \mathbf{F}_{(R,S)}^{-1}(\boldsymbol{x}_0' + \mathbf{d}^S).$$

By the fundamental theorem of calculus

$$\tilde{\mathbf{d}}^S = \boldsymbol{x}(1) - \boldsymbol{x}(0) = \int_0^1 \frac{d\boldsymbol{x}(\theta)}{d\theta} d\theta$$

$$= \int_0^1 J^{-1}(\boldsymbol{x}(\theta)) \frac{d\boldsymbol{x}'(\theta)}{d\theta} d\theta$$
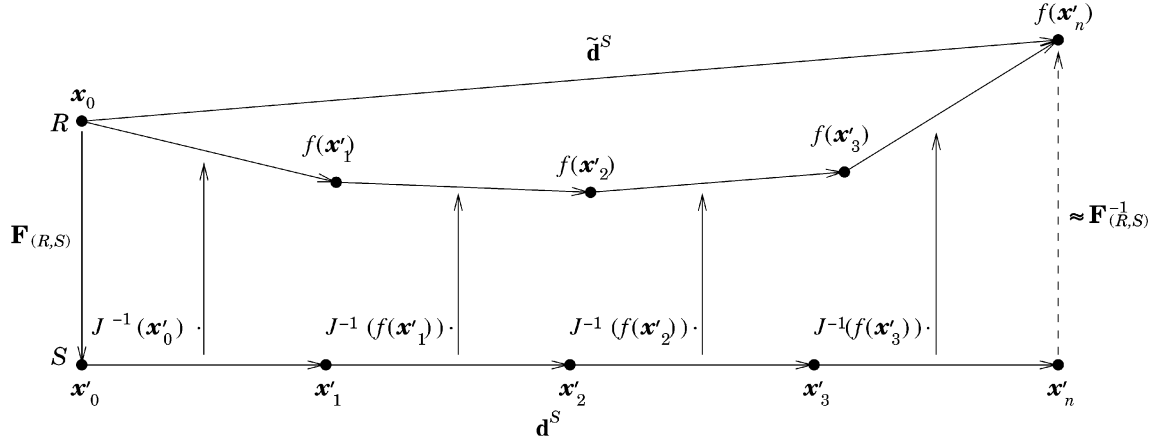
Fig. 1. This figure shows how the transformed vector at the point with reference coordinates $\boldsymbol{x}_0$ is determined using the recursion formula. First, $\mathbf{F}_{(R,S)}$ is used to map into the source coordinate system giving $\boldsymbol{x}'_0$, and the untransformed motion vector $\mathbf{d}^S$ at this location is then divided into n intervals. In this case, we have set $n = 4$. Each interval is then transformed using the Jacobian matrix evaluated at the current location expressed in R coordinates, and on each occasion, the transformed interval is appended to the current position to give the new position in R coordinates. Once all intervals have been transformed, the final R coordinates $f(\boldsymbol{x}'_n)$ enable the transformed motion vector $\tilde{\mathbf{d}}^S$ to be calculated.

where $\boldsymbol{x}'(\theta)$ is $\mathcal{L}$ defined in the coordinate system of S representing the untransformed motion vector $\mathbf{d}^S$ and $J(\boldsymbol{x}(\theta))$ is the Jacobian matrix of the transformation $\mathbf{F}_{(R,S)}$ evaluated along $\boldsymbol{x}(\theta)$

$$ J = \begin{bmatrix} \frac{\partial x'}{\partial x} & \frac{\partial x'}{\partial y} & \frac{\partial x'}{\partial z} \\ \frac{\partial y'}{\partial x} & \frac{\partial y'}{\partial y} & \frac{\partial y'}{\partial z} \\ \frac{\partial z'}{\partial x} & \frac{\partial z'}{\partial y} & \frac{\partial z'}{\partial z} \end{bmatrix}_{\boldsymbol{x}=\boldsymbol{x}(\theta)} $$

which can be determined analytically. This integral can then be approximated by dividing the interval $[0, 1]$ into n subintervals of length $1/n$

$$ \tilde{\mathbf{d}}^S \simeq \sum_{k=0}^{n-1} J^{-1}(\boldsymbol{x}^{(k)})(\boldsymbol{x}'^{(k+1)} - \boldsymbol{x}'^{(k)}) $$

where $\boldsymbol{x}'^{(k)} = \boldsymbol{x}'_0 + (k/n)\mathbf{d}^S$ and $\boldsymbol{x}^{(k)} = \mathbf{F}_{(R,S)}^{-1}(\boldsymbol{x}'^{(k)})$. In a previous publication [22], we used precisely this formulation but with $n = 1$. We improved the approximation to the integral in a later publication [23] by setting $n > 1$ and evaluating the integral as

$$ \tilde{\mathbf{d}}^S = \boldsymbol{f}(\boldsymbol{x}'^{(n)}) - \boldsymbol{x}_0 $$

where $\boldsymbol{f}$ is the recursion formula

$$ \begin{aligned} \boldsymbol{f}(\boldsymbol{x}'^{(0)}) &= \boldsymbol{x}_0 \\ \boldsymbol{f}(\boldsymbol{x}'^{(k+1)}) &= \boldsymbol{f}(\boldsymbol{x}'^{(k)}) + J^{-1}(\boldsymbol{f}(\boldsymbol{x}'^{(k)}))(\boldsymbol{x}'^{(k+1)} - \boldsymbol{x}'^{(k)}) \\ & k = 0, \ldots, n-1. \end{aligned} $$

Fig. 1 illustrates the mechanism of the recursion formula described. In the base step, the intersubject mapping is used to transform from R coordinates $\boldsymbol{x}_0$ into S coordinates $\boldsymbol{x}'_0$. The untransformed motion vector $\mathbf{d}^S$ at this location is then divided into n intervals to give S coordinates $\boldsymbol{x}'_1, \ldots, \boldsymbol{x}'_n$. At each recursive step k, the next interval $\boldsymbol{x}'^{(k+1)} - \boldsymbol{x}'^{(k)}$ is transformed into the coordinate system of R and the resulting vector is appended to $\boldsymbol{f}(\boldsymbol{x}'^{(k)})$ to give the new position $\boldsymbol{f}(\boldsymbol{x}'^{(k+1)})$. Once all intervals have been transformed, we arrive at $\boldsymbol{f}(\boldsymbol{x}'^{(n)})$ which is our approximation to the coordinates $\mathbf{F}_{(R,S)}^{-1}(\boldsymbol{x}'_0 + \mathbf{d}^S)$. The transformed vector $\tilde{\mathbf{d}}^S$ is then given by $\tilde{\mathbf{d}}^S = \boldsymbol{f}(\boldsymbol{x}'^{(n)}) - \boldsymbol{x}_0$.

Applying this technique to each of the motion/deformation fields of the subject S gives us a set of transformed motion fields $\tilde{\mathbf{D}}_{(0,i)}^S(x, y, z)$. Transforming our field in this way produces a field that is said to be conjugate to the original field (see the Appendix).

III. RESULTS AND DISCUSSION

A. Nonrigid Registration

Although both the motion/deformation fields as well as the intersubject mappings can be calculated or produced using any registration technique, in this paper we calculate both using the nonrigid registration technique of Rueckert *et al.* [24]. This algorithm expresses the required transformation as the sum of a global and local component

$$ \mathbf{T}(x, y, z) = \mathbf{T}_{\text{global}}(x, y, z) + \mathbf{T}_{\text{local}}(x, y, z). $$

$\mathbf{T}_{\text{global}}$ is modeled by an affine transformation that incorporates scaling, shearing, rotation, and translation. $\mathbf{T}_{\text{local}}$, the local deformations, are modeled using a free-form deformation (FFD) model based on B-splines that manipulates an underlying mesh of control points ϕ, thus changing the shape of the object. The resulting deformation can be expressed as the three-dimensional (3-D) tensor product of the standard one-dimensional cubic B splines

$$ \mathbf{T}_{\text{local}}(x, y, z) = \sum_{l=0}^{3} \sum_{m=0}^{3} \sum_{n=0}^{3} B_l(u) B_m(v) B_n(w) \phi_{i+l, j+m, k+n} $$

where B_l denotes the l-th B-spline basis function. To find the parameters of the transformation $\mathbf{T}$ the algorithm uses a voxel-based similarity measure, normalized mutual information [25], which measures the degree of alignment between images. The normalized mutual information of two images A and B is defined as

$$ \mathcal{I}(A, B) = \frac{\mathcal{H}(A) + \mathcal{H}(B)}{\mathcal{H}(A, B)} $$

where $\mathcal{H}(A)$, $\mathcal{H}(B)$ are the marginal entropies of images A and B, and $\mathcal{H}(A, B)$ denotes the joint entropy of the combined images A, B. The entropies are calculated using a two-dimensional
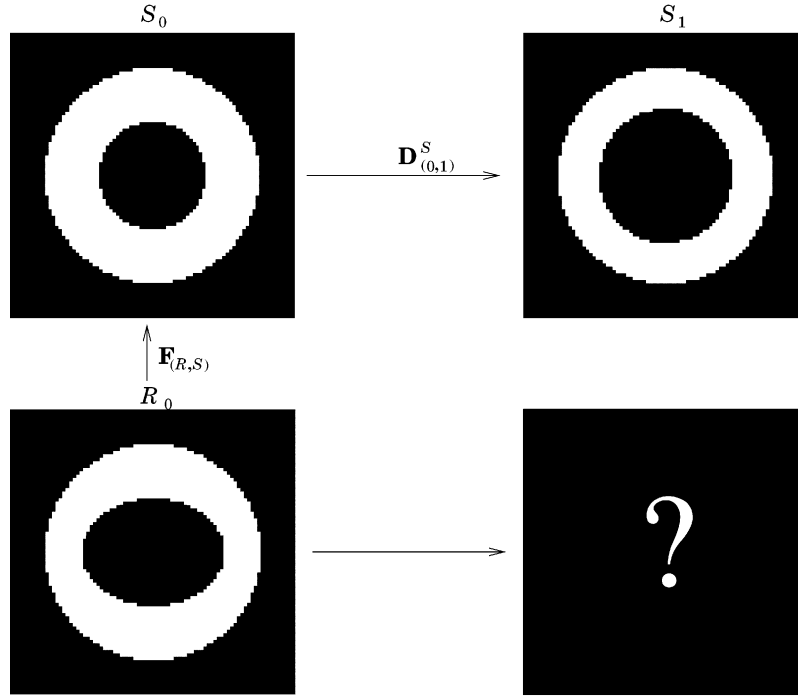
Fig. 2. Images S_0 and R_0 show corresponding 2-D views of the synthetic subject and reference at time $t = 0$, while S_1 shows the deformed subject at time $t = 1$. We need to transform the deformation field of S, $\mathbf{D}^S_{(0,1)}$, into the coordinate system of R to give the corresponding deformation field for the reference subject.

(2-D) histogram to estimate the corresponding probability density functions. We are using normalized mutual information as a similarity measure because it only measures the statistical dependencies between the intensity distributions in both images rather than the actual intensity values themselves. This becomes important in Section III-C where we use this nonrigid image registration algorithm to track the heart in a sequence of tagged MR images where the image intensities can change as a result of tag fading.

As mentioned in Section II-B we assume that the transformation between reference and subject coordinate systems is diffeomorphic. To ensure that the FFD calculated by the nonrigid registration algorithm is diffeomorphic we have added a second term to the cost function that penalises any nondiffeomorphic transformations using the following penalty function $\mathcal{P}$:

$$\mathcal{P} = \begin{cases} \frac{|J(x,y,z)|^2}{\gamma^2} + \frac{\gamma^2}{|(J(x,y,z)|^2} - 2, & \text{if } |J(x,y,z)| \leq \gamma \\ 0, & \text{otherwise} \end{cases}.$$

Here $|J(x,y,z)|$ represents the determinant of the Jacobian of the FFD. A similar penalty function has been first proposed by Edwards et al. [26] and effectively penalises any transformations for which the determinant of the Jacobian falls below a threshold γ. By penalising Jacobians that approach zero, we prevent the transformation from collapsing and keep it diffeomorphic. Note that simply using a smoothness penalty function would not be sufficient to guarantee a diffeomorphic transformation, since it is possible for a transformation to be smooth but nondiffeomorphic.

The cost function $\mathcal{C}$ which the registration algorithm minimizes is a combination of the image similarity $\mathcal{I}$ and the penalty function $\mathcal{P}$

$$\mathcal{C} = -\mathcal{I} + \lambda \mathcal{P}.$$

The weighting parameter λ defines the tradeoff between the image similarity and the penalty function. For the experiments in this paper, γ was set to 0.3 and λ to 0.1.

B. Validation With Synthetic Data

For the purposes of validation, we have generated synthetic 3-D images to which we applied our proposed transformation algorithm. First, a synthetic image S_0 was generated depicting the anatomy of a subject S at time $t = 0$. In this case, the anatomy was modeled as a sphere with a spherical inner wall surface centred on the object centre, giving a wall of homogeneous thickness. A pattern was also imposed throughout the wall to add texture information. We show a 2-D slice of this image in the top left corner of Fig. 2 without the texture information. The synthetic 3-D image was then transformed using a known mapping that had been interpolated using a B-spline model to produce the corresponding 3-D image R_0 that depicts the reference subject R at time $t = 0$. The mapping used retains the spherical outer surface, but deforms the inner wall in the x-direction so that the wall no longer has constant thickness. We show a 2-D slice of this image in the bottom left corner of Fig. 2. To generate a motion for the anatomy of subject S we once again used a known mapping expressed with a B-spline model to transform S_0 to an image S_1 representing the deformed version of S at time $t = 1$. This transformation is a uniform outward radial movement of the inner surface of S that linearly falls to zero at the outer wall of S. Again a 2-D slice of this image is shown in the top right corner of Fig. 2. Our goal is to calculate the corresponding deformation in the coordinate system of the reference subject R. Since the motion of the image S_0 is one in which each point on the inner wall moves an equal distance toward the outer wall, we would expect the transformed motion field in the reference
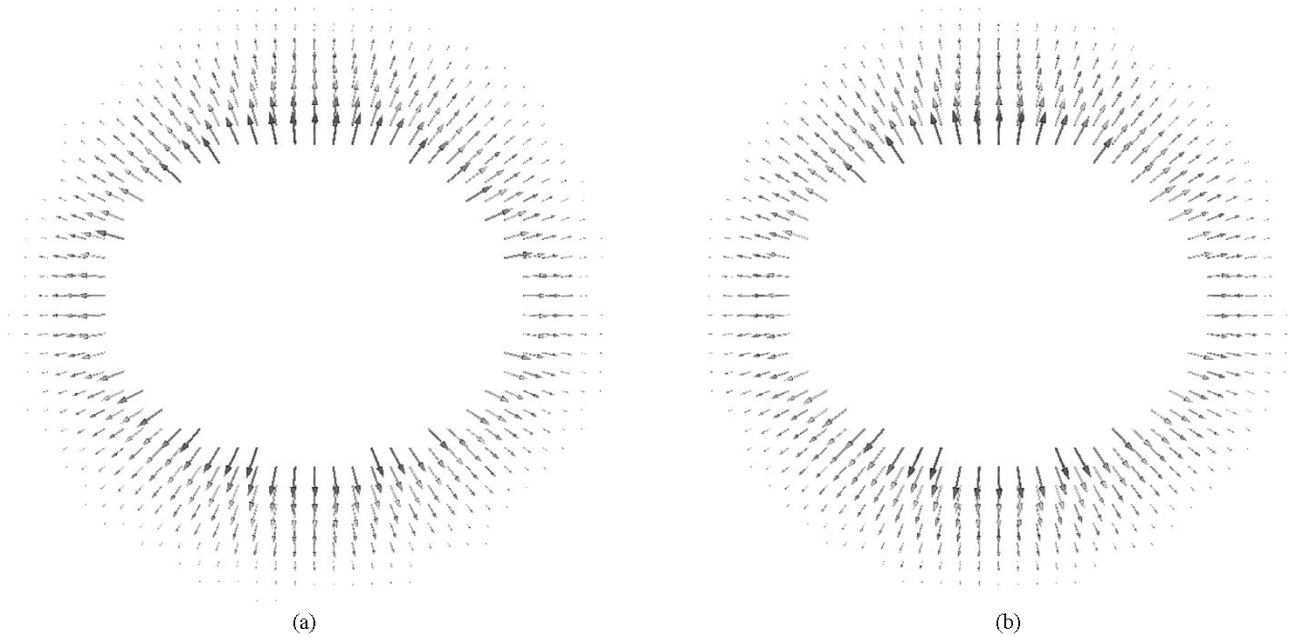
Fig. 3. The calculated transformed motion field of the subject with homogeneous wall thickness into the coordinate system of the reference is shown in (a). (b) Shows what the transformed motion field should look like.

coordinate system to be of similar magnitude to the original motion field where the wall thickness of each subject is similar, but to be relatively smaller at those points of the reference subject at which the wall is thinner.

The motion field of subject S was calculated by registering S_0 to S_1 and deriving the motion field $\mathbf{D}_{(0,1)}^S$ as explained in Section II-A. The intersubject mapping $\mathbf{F}_{(R,S)}$ is calculated by registering R_0 to S_0, and the field $\mathbf{D}_{(0,1)}^S$ was then transformed using this mapping and the recursion formula described in Section II-B. We set $n = 4$ when applying the recursion formula to produce the transformed field $\tilde{\mathbf{D}}_{(0,1)}^S$ shown in Fig. 3(a). Since all mappings in this example are known *a priori*, we can also determine the theoretical transformed motion field shown in Fig. 3(b) without doing any registrations or numerical inverse approximation. We can see that the calculated and the theoretical transformed motion fields are almost identical and in fact the root-mean-square (rms) difference between these two fields is 0.08 pixels, with a maximum error of 0.42 pixels. These figures compare favorably with the rms deformation and the maximum deformation of the theoretical transformed field which are 1.47 pixels and 3.92 pixels, respectively, demonstrating that the numerical errors that accumulate during the registrations and numerical inverse approximation are of a negligible size. We can improve the overall accuracy of our method by using a larger value of n when using the recursion formula, since, up to a point, this improves the numerical approximation to the inverse that we calculate. For example, with $n = 10$ the rms error is 0.08 pixels and the maximum error is 0.36 pixels. Conversely, if we reduce the value of n to 1, the accuracy degrades to an rms error of 0.1 pixels and a maximum error of 0.79. However, it is interesting to note that with $n = 100$, the errors to two decimal places are the same as those when $n = 10$. The reason for this lies in the way our recursive technique works (see Section II-B) when trying to approximate $\mathbf{F}_{(R,S)}^{-1}(\boldsymbol{x}_0' + \mathbf{d}^S)$ so that we may calculate the transformed vector at $\boldsymbol{x}_0$. Each time the recursion function

f is recursively applied, a point $\boldsymbol{x}_k'$ that lies closer to $\boldsymbol{x}_0' + \mathbf{d}^S$ than the preceding point $\boldsymbol{x}_{k-1}'$ is transformed to R coordinates to give $f(\boldsymbol{x}_k') \approx \mathbf{F}_{(R,S)}^{-1}(\boldsymbol{x}_k')$. This is calculated using the Jacobian evaluated at $f(\boldsymbol{x}_{k-1}') \approx \mathbf{F}_{(R,S)}^{-1}(\boldsymbol{x}_{k-1}')$ but since this is only an approximation, the numerical error will be passed on to the calculation of $f(\boldsymbol{x}_k')$. The final value $f(\boldsymbol{x}_n') \approx \mathbf{F}_{(R,S)}^{-1}(\boldsymbol{x}_0' + \mathbf{d}^S)$ will, therefore, have errors that accumulate at every step of the recursion scheme, i.e., n times. For very large n, there will be some tradeoff between improvements in accuracy due to an increased number of intervals used to approximate the integral, and lowering in accuracy due to an accumulation of errors attributed to the recursive nature of the inversion scheme. In addition, larger values of n also lead to increased computational time. Throughout this paper we have used $n = 4$ since this seems to represent a reasonable compromise between the numerical accuracy and computational time required.

C. Application to Cardiac MR Images

To test our proposed method on real data we applied our technique to transform the motion fields describing the cardiac motion of a set of subjects into the coordinate system of a single reference subject. In order to calculate the motion fields of the subjects we used images acquired using tagged MR [6], [7] which provides a means to investigate the deformations that the heart undergoes through the cardiac cycle. Tagged MR images are produced by perturbing the magnetization in the myocardium in a specified spatial pattern at end-diastole, i.e., when the heart is at peak relaxation. These appear as dark stripes or grids when imaged immediately after the application of the tag pattern, and, since the myocardial tissue retains this perturbation, the dark stripes or grids deform with the heart as it contracts, allowing local deformation parameters to be estimated. To calculate the myocardial motion fields we are using an extension of the FFD model described in Section III-B in which a

$$S_0 \qquad\qquad S_1 \qquad\qquad S_n$$

$$\mathbf{T}^{S}_{(0,1)}$$

$$\mathbf{T}^{S}_{(0,n)} = \sum_{j=0}^{n-1} \mathbf{T}^{S}_{(j,j+1)}$$
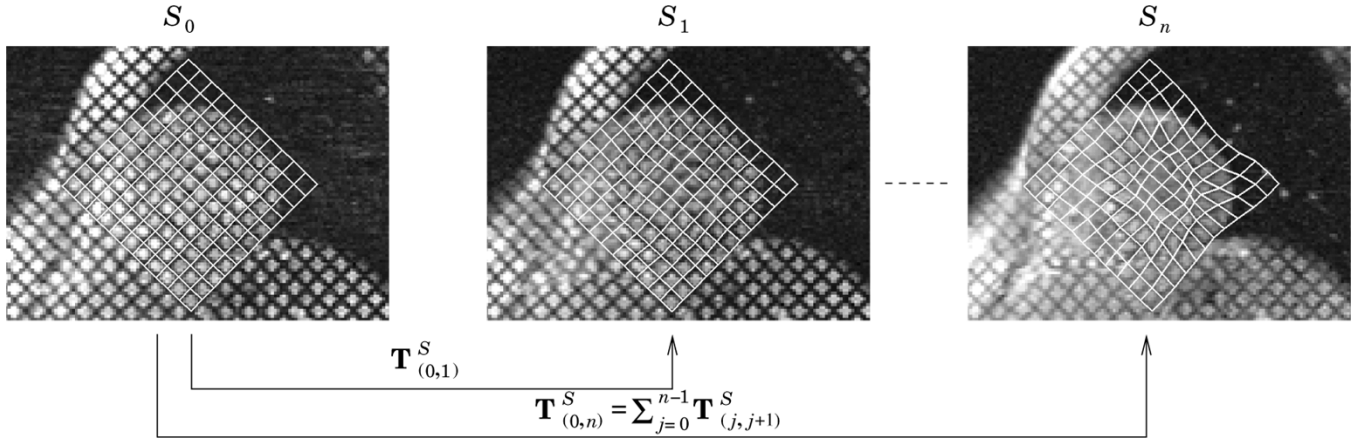
Fig. 4.   Extraction of cardiac motion parameters: A virtual tag grid which has been aligned with the tag pattern at time $t = 0$ is overlaid on different time frames of the tagged MR sequence to illustrate the tag tracking with nonrigid registration. As time progresses the virtual tag grid is deformed by the motion field calculated by the nonrigid registration and follows the underlying tag pattern in the images. An animated color version of this figure can be found at http://www.doc.ic.ac.uk/~dr/research/CardiacMotionTracking.html.

number of single-level FFDs are combined in a multi-level FFD framework [27]. In order to compute a 3-D motion field the algorithm aligns both the end-diastolic short-axis and long-axis tagged MR images at time $t = 0$ to their corresponding images at each time frame $t = i$. The transformation between the end-diastolic time frame S_0 and the image S_i at time frame $t = i$ is then given by

$$\mathbf{T}^{S}_{(0,i)}(x', y', z') = \sum_{j=0}^{i-1} \mathbf{T}^{S}_{(j,j+1)}(x', y', z').$$

This approach has been previously applied successfully for myocardial motion tracking [5], [28]. Fig. 4 shows the short axis tagged images taken at different time frames overlayed with a virtual grid which has been aligned with the tag pattern of the end-diastolic frame. As time progresses, the virtual tag grid is deformed by the motion field calculated from the nonrigid registration and follows the underlying tag pattern in the images. This provides a visual assessment of the success of the tracking algorithm. The motion fields $\mathbf{D}^{S}_{(0,i)}(x', y', z')\ i = 1, \ldots n$ associated with the calculated transformations are then determined as described in Section II-A. The motion field $\mathbf{D}^{R}_{(0,i)}(x, y, z)\ i = 1, \ldots n$ of subject R is calculated in the same manner using the tagged image sequences of this subject.

In addition, we also require the mapping between subjects R and S to transform the motion fields of S into the coordinate system of R. To do this, we acquired a set of untagged images for all subjects shortly after the acquisition of the tagged images. The short-axis images are acquired in the same position as the tagged images and do have the same spatial and temporal resolution. This means that we can use the end-diastolic untagged images from each subject, to calculate the intersubject coordinate system mapping. The transformation between subjects R and S is determined using the nonrigid registration algorithm described in Section III-B, giving a mapping $\mathbf{F}_{(R,S)}$ between coordinate systems (x, y, z) and (x', y', z'). The technique described in Section II-B is then used to transform the motion fields of S into the coordinate system of R giving the fields $\tilde{\mathbf{D}}^{S}_{(0,i)}(x, y, z)$.

We applied our technique using sets of untagged and tagged short-axis images of nine healthy volunteers. The untagged and tagged MR images were acquired shortly after each other to minimize any motion between the image acquisitions. All images were acquired using a Siemens Sonata 1.5T scanner. For the tagged sequences, a cine breath-hold sequence with a SPAMM tag pattern was used to acquire ten short-axis slices covering the entire LV and a set of long-axis slices. For the untagged images, a cine breath-hold TrueFisp sequence was used to acquire ten slices in the same anatomical planes as the tagged imaging planes. In both cases, the images have a resolution of 256×256 pixels with a field of view ranging between 300 and 350 mm depending on the subject and a slice thickness of 10 mm. Imaging was done at the end of exhalation and all images have been visually assessed to verify that there was minimal motion between the acquisitions. Our previous experiments [5] have shown that, using a manual tag tracking as the gold standard, the nonrigid registration algorithm is able to track the myocardial motion with an rms error of less than 0.5 mm in simulated data and with an rms error between 1 and 2 mm on tagged MR images. One of the nine subjects was used as reference subject, and the untagged end-diastolic images of the other were registered to this one using a mesh with a uniform control point spacings of 5 mm. The calculated transformations were then used to map the myocardial motion fields of each of these eight subjects into the coordinate system of the reference subject.

The principal reason for the transformation of the cardiac motion fields into a common coordinate system is that it enables the motion patterns of the different subjects to be compared and analyzed both qualitatively and quantitatively. To demonstrate this approach we have constructed an atlas of cardiac motion by averaging the transformed motion fields: Given the motion fields of k subjects $S^0, S^1, \ldots, S^{k-1}$ and a reference subject R the average motion field $\mathbf{A}_{(0,i)}(x, y, z)\ i = 1, \ldots n$ is calculated as [23]

$$\mathbf{A}_{(0,i)}(x, y, z) = \frac{1}{k+1}\left(\mathbf{D}^{R}_{(0,i)}(x, y, z) + \sum_{j=0}^{k-1} \tilde{\mathbf{D}}^{S^j}_{(0,i)}(x, y, z)\right).$$
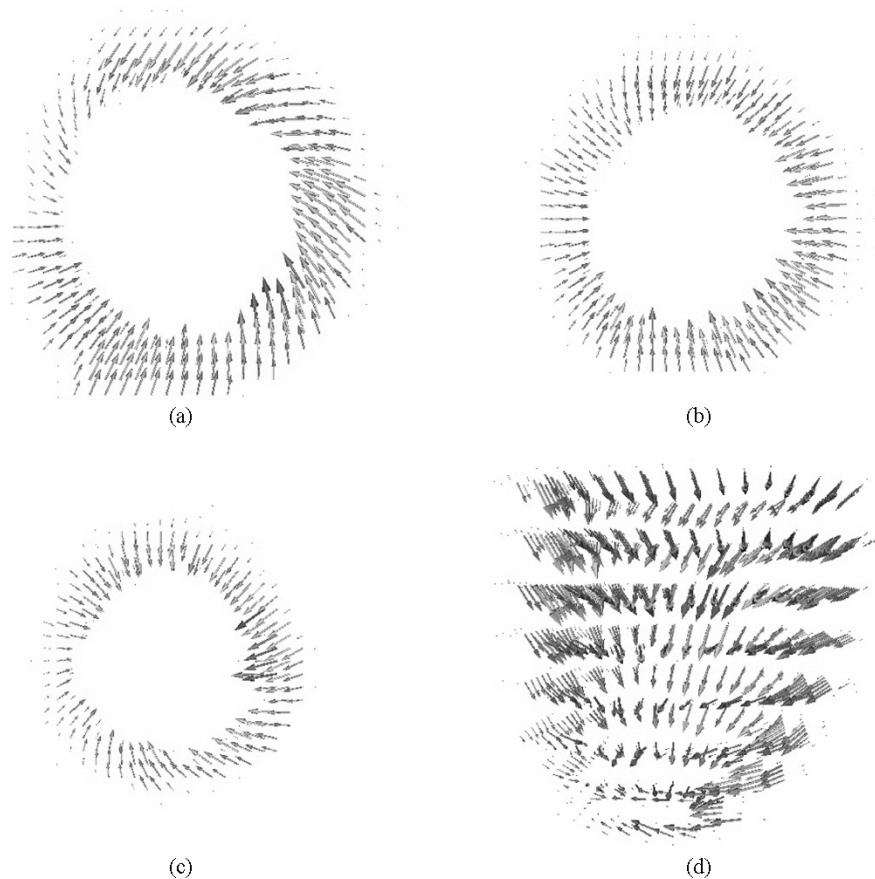
Fig. 5. The myocardial motion field at end-systole of the cardiac atlas on a short-axis slice toward the base of the left ventricle is shown in (a). (b) and (c) Corresponding motion fields for parallel slices through the middle of the left ventricle and toward the apex of the left ventricle, respectively. (d) Motion field from a long-axis side view of the left ventricle. In cases (a)-(c), the motion fields have been projected onto the planes defined by the associated anatomical slice, whereas all three components of the motion field are shown in (d). Full color animations of these fields can be found at http://www.doc.ic.ac.uk/~dr/IEEE_TMI/DeformationAtlas.html.

We have calculated such an atlas using the transformed motion fields of our 8 subjects and our reference subject R. Since each of the datasets were acquired from volunteers, the atlas represents the average motion model of the hearts of this population.

Fig. 5 shows the calculated cardiac motion atlas describing cardiac motion between end-diastole and end-systole. We chose to show the motion fields at end-systole because this is when the deformation of the heart is greatest, and vectors are only shown for regions which are part of the myocardium. Fig. 5(a) shows a short-axis slice toward the base of the left ventricle of the heart, Fig. 5(b) shows a slice through the middle of the left ventricle, Fig. 5(c) shows a slice toward the apex of the left ventricle, while Fig. 5(d) shows a long-axis side view of the heart. The magnitude of the motion vectors is indicated by the length of the arrows. In Fig. 5(a)-(c), the motion fields have been projected onto the planes defined by the associated anatomical slice, while all three components of the motion field are shown for Fig. 5(d). All of the slices show a contraction of the left ventricle but we can also see that toward the base of the heart the atlas has a counter-clockwise twisting action while toward the apex it has a clockwise twist. The motion in the slice through the middle of the left ventricle has minimal twisting and is almost a pure contraction. These observations confirm that our motion atlas possesses the characteristic qualitative behavior that we would expect in a healthy heart.

D. Application to Brain MR Images

To demonstrate the flexibility of the proposed technique we have applied it to a set of deformation fields describing the structural changes over time in the brains of a series of subjects. These deformation fields have then been mapped into a common coordinate system of a single reference subject. For this purpose, MR brain data sets of 19 different subjects were acquired, each of whom were diagnosed with first-episode schizophrenia with less than 12 weeks lifetime exposure to anti-psychotic medication. Scanning was performed on a 1.5T Eclipse MR system (Phillips Medical Systems), giving images with a resolution of 256×256 pixels with a slice thickness of 1.6 mm and a field of view of 250 mm. For each subject, an image was acquired at time $t = 0$ and at time $t = 1$, with the average time interval being 8 months [29].

In the first step, the deformation fields between the baseline and followup scans were calculated using the nonrigid registration algorithm described in Section III-B. Since the MR scanner produces high resolution images with good soft tissue contrast, the deformation fields allow us to investigate how different regions of the brain change in size and shape between baseline and followup times. Although in our example each subject data set consists of images acquired on just two different occasions, one could calculate and transform the deformations describing brain
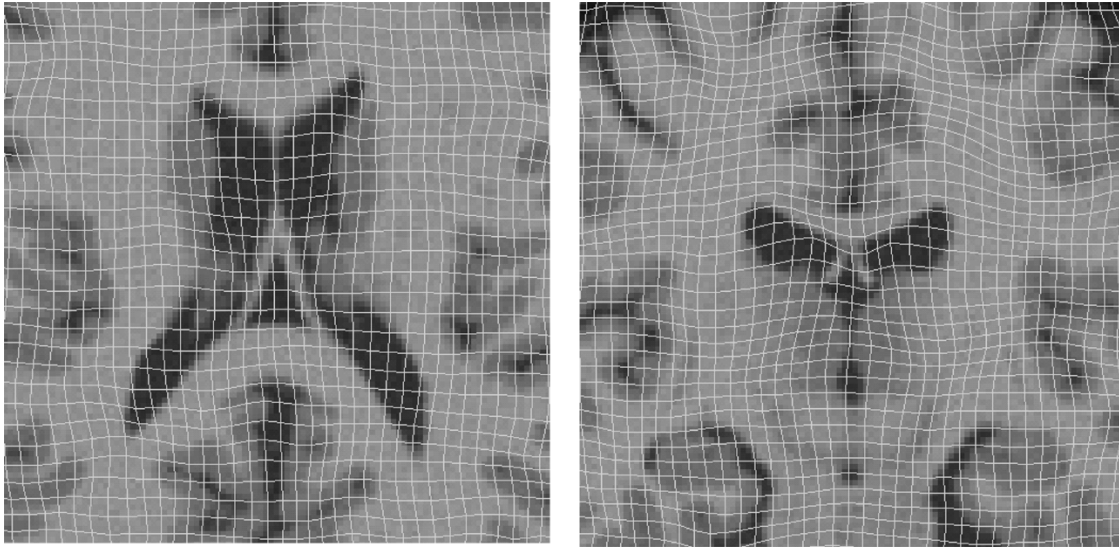
Fig. 6. The deformation grid of the brain deformation atlas constructed in Section III-D.
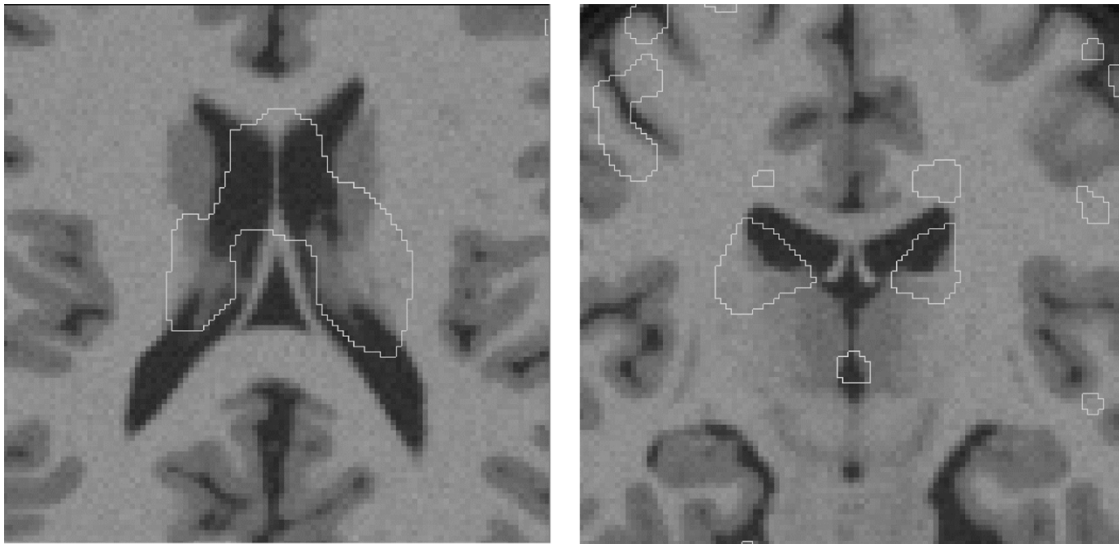

Fig. 7. This figure shows the isoline of the volume change function of the brain deformation atlas constructed in Section III-D corresponding to a 2% volume expansion. A full color version of the volume change map can be found at http://www.doc.ic.ac.uk/~dr/IEEE_TMI/DeformationAtlas.html.

deformations at many more time points if the corresponding images are available. In the second step, the baseline MR images of all subjects were registered to a reference brain based on the MNI brainweb dataset [30] using again the nonrigid registration algorithm described in Section III-B. The intersubject mappings were then used to map the deformation fields of each of the 19 subjects into the coordinate system of the MNI brainweb reference subject.

Analogous to the cardiac example in Section III-C, we then produced a brain deformation atlas $\mathbf{A}_{(0,1)}(x, y, z)$ using the transformed deformation fields of our 19 subjects. Since each of the subjects has been diagnosed with first-episode schizophrenia, the resulting atlas represents the expected temporal deformations of a brain in patients with first-episode schizophrenia defined in the coordinate system of the reference. Axial and coronal slices through the resulting deformation atlas are shown on the left and right, respectively, of Fig. 6. This atlas is much more difficult to interpret directly than the cardiac atlas

because the long-term deformations of the brain are much more subtle and appear to be less coherent than the transient motion that the heart undergoes over the cardiac cycle. One way of analysing this field is to perform a volume-change analysis of the deformation by calculating its associated volume change function, which can then be visualised as a scalar image. The volume change function of a transformation

$$\mathbf{T}^S(x, y, z) = (x'(x, y, z), y'(x, y, z), z'(x, y, z))$$

is calculated as

$$\Phi_{\mathbf{T}}(x_0, y_0, z_0) = \mathrm{Det} \begin{bmatrix} \frac{\partial x'}{\partial x} & \frac{\partial x'}{\partial y} & \frac{\partial x'}{\partial z} \\ \frac{\partial y'}{\partial x} & \frac{\partial y'}{\partial y} & \frac{\partial y'}{\partial z} \\ \frac{\partial z'}{\partial x} & \frac{\partial z'}{\partial y} & \frac{\partial z'}{\partial z} \end{bmatrix}_{(x_0, y_0, z_0)}$$

and represents the local volume scaling factor of the transformation at each point (x_0, y_0, z_0). Since the deformation atlas $\mathbf{A}$

is an average of the transformed deformation fields, the volume-change function of this atlas $\Phi_\mathbf{A}$, therefore, gives the volume-change of the average transformed deformation field (which we call VATD). Fig. 7 shows the isoline corresponding to an expansion of 2% of the resulting volume-change function for the same slices as shown in Fig. 6. The image seems to indicate an expansion of the ventricles as time progresses. Similar observations using this data have been reported previously in [29].

Alternatively, one can perform a similar volume-change analysis without transforming the deformation fields of each subject to the reference. This is achieved by calculating for each subject the volume-change functions from the untransformed deformation fields in their native coordinate system and then mapping them in the coordinate system of the reference subject by simply applying the intersubject maps to the images of the corresponding volume-change functions. These transformed images are then averaged to produce an image which, therefore, represents the average of the transformed volume changes of the deformation of each subject (ATVD). Such an image would not be identical to the VATD image shown in Fig. 7 for a number of reasons. In particular, the volume change function corresponds to the determinant of a matrix and, thus, is not a linear operator. Hence, the volume change of an average field is not the same as the average of the volume changes in a series of fields. However, even if we examine the images produced using both approaches for a single subject, i.e., without averaging over a series of subjects, there will still be differences. Fig. 8(a) shows the isoline corresponding to a 2% expansion of the transformed volume change of the original deformation field of one of the schizophrenic subjects while Fig. 8(b) shows the corresponding isoline of the volume change of the transformed deformation field of the subject. We can see that the two images are not identical and this is because of the way that the volume-change of the original untransformed deformation field is placed in the coordinate system of R. By treating the volume-change function as an "image" rather than gradient of deformation operator (which is what it is), its transformation into the coordinate system of R only places the volume-change values in the correct anatomical location of the reference subject, without changing the values themselves to correct for the coordinate system differences between subject and reference (see the Appendix). Such a function as that shown in Fig. 8(a) is, therefore, a "half-transformed" volume change function when compared to the volume change function of Fig. 8(b). As we show in the Appendix , the "half-transformed" volume-change function in Fig. 8(a) can be fully transformed into the coordinate system of R by multiplying the values at each point by a scaling factor that depends on the point location, the transformed deformation field, and the reference-to-subject mapping. Applying this volume-correction to the volume-change function of Fig. 8(a) gives a new volume-change function, and we show the isoline corresponding to a 2% expansion of this function in Fig. 8(c). We can see that this image is now very similar to that shown in Fig. 8(b).

Moreover, the brain deformation atlas approach is much more useful because while both the VATD and the ATVD images are scalar valued and, therefore, of limited use, the atlas $\mathbf{A}$ contains multidimensional deformation information that can be analyzed further. For example, one can analyze the directions of the volume changes using the brain deformation atlas, which
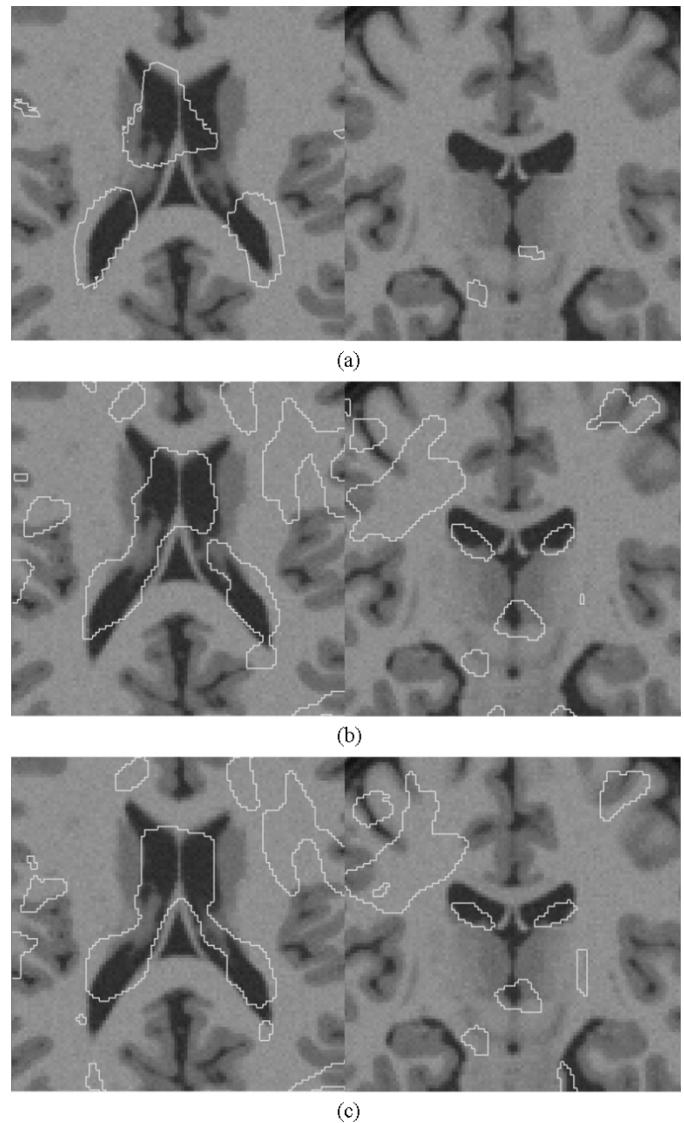

(a)

(b)

(c)

Fig. 8. Isolines corresponding to a 2% expansion of the volume change maps of a single subject calculated using the ATVD and VATD methods. (a) Isoline of the volume change using the ATVD approach. (b) Isoline of the volume change using the VATD approach. (c) Isoline of the function shown in (a) after the volume correction (discussed in the Appendix). Full color versions of the volume change maps can be found at http://www.doc.ic.ac.uk/~dr/IEEE_TMI/DeformationAtlas.html.

one cannot do using either of the volume-change images because it is impossible to reconstruct a unique deformation field from just the volume-change function of the field.

IV. CONCLUSION AND FUTURE WORK

In this paper, we have developed a technique that can be used to transform motion and deformation fields defined in one coordinate system into another coordinate system. Such a transformation of the fields of a series of subjects into the coordinate system of a single reference subject facilitates their analysis and comparison by accounting for the differences in size and shape of the subjects. The proposed method can, therefore, be useful in a wide range of clinical scenarios. In Section III-C, we described how it can be used to build a cardiac motion atlas that represents an average healthy heart motion by transforming

the motion fields of a number of subjects into a single reference coordinate system and then averaging them. The motion of the resulting atlas was shown to possess the characteristic qualitative behavior that we would expect in a healthy heart. In the same spirit we have shown in Section III-D how the proposed method can be used to build a brain deformation atlas that contains the expected long-term deformations that occur in the brains of schizophrenics by transforming the deformation fields of a number of subjects into a single reference coordinate system and then averaging them. A volume change analysis of the resulting atlas appeared to show that the ventricles in a schizophrenic subject expand over time. There are other possible applications of the motion and deformation field transformation technique presented in this paper: For example, Chandrashekara *et al.* [28] have performed a principal component analysis of the transformed cardiac motion fields of a number of subjects and then used the recovered principal modes to guide the motion tracking algorithm described in Section III-C. These principal modes could also be incorporated into the cardiac atlas to extend it from a simple mean motion model to one in which a range of types of motion for a particular population can be produced.

There are some theoretical and practical considerations regarding the use of our field transformation technique to transform the field of one subject into that of a reference subject: In particular, the choice of the reference subject itself will be important for two reasons. First, by changing the reference subject we will change the transformed field as the intersubject mapping will then be different. This means that if we wish to compare the transformed fields of a number of different subjects there will be some bias associated with the choice of reference subject. For example, one choice of reference subject may appear to give very similar (in terms of vector difference) transformed fields across the different subjects for a particular section of the reference, while another choice of reference may give a much larger variation in the transformed fields for the corresponding section of that reference. Note that any bias is quantitative rather than qualitative as it is the vector differences that will differ with choice of reference subject; the qualitative descriptions of the transformed motion/deformations will be the same with any choice of reference subject. This is because the transformed motion/deformation fields will always be conjugate to the original untransformed field whichever reference subject is chosen, and since conjugacy is an equivalence relation, each transformed field will be conjugate to each other. This means that if one transformed field indicates, for example, a swapping in the positions of two anatomical regions, then the other transformed field will indicate the same swapping even though the fields themselves will be numerically different. Since there is no way to remove the quantitative bias, the best that one can do is to choose a reference subject that is representative of the subject population as a whole, i.e., one whose anatomy lies toward the centre rather than at the extrema of the distribution of anatomies of the subject population. This then enables us to draw meaningful quantitative conclusions from the set of transformed fields. For the heart and the brain applications described in this paper, we did indeed try to choose such reference subjects, but this was done purely by visual assessment. A better approach would be to calculate an "average" shape using the subject population and use this as the reference subject. The choice of the reference subject is important for a second reason:

Since our method relies on calculating the inverse of the intersubject mapping in order to transform the field of one subject into the coordinate system of a reference subject, the technique is ill-posed if no such inverse exists. Such an inverse will exist if the intersubject mapping is always one to one and onto, i.e., if every point of the anatomical region of interest in each subject corresponds with a unique point in the other subject. In addition, the numerical technique used to determine the inverse requires the calculation of the Jacobian matrix of the original mapping, which implicitly assumes the intersubject mapping to be differentiable and, therefore, smooth and topology preserving. The reference subject chosen must, therefore, not only contain "the same" anatomy as the other subject, but also have the same topology. In the case of the heart application described in Section III-C, both of these assumptions are reasonable ones to make since all subjects were healthy and so we expect to be able to make a one-to-one and onto point correspondence between each subject that preserves the topology. However, for the brain application described in Section III-D these assumptions are more problematical. It is known that even the brains of healthy subjects can be topologically different, which raises doubts about the topological equivalence of the schizophrenic brains used to calculate the atlas. Although we side-stepped this problem by ensuring the invertibility and the topology preservation of the intersubject mappings by including a penalty energy term during the registrations (see Section III-A), this is an important issue that is difficult to resolve. For example, how does one transform the deformations of a particular structure found in one brain into the coordinate system of another brain that does not contain that structure? This is a question that we will address in future work. Finally, it should be noted that our transformation method is fundamentally a numerical inversion technique and that although the errors are of a neglible size, improvements in the numerical accuracy of the inverse mapping would certainly prove beneficial.

APPENDIX

A map $g : X \subseteq \Re^n \longmapsto \Re^n$ is said to be conjugate to the map $f : X' \subseteq \Re^n \longmapsto \Re^n$ iff there exists a homomorphism, i.e., a 1–1 onto map $F : X \longmapsto X'$ such that

$$g(x) = F^{-1}(f(F(x))).$$

If we associate each of the transformed motion fields $\tilde{\mathbf{D}}^S_{(0,i)}(x, y, z)$ for a subject S with a mapping

$$\tilde{\mathbf{T}}^S_{(0,i)}(x, y, z) = (x, y, z) + \tilde{\mathbf{D}}^S_{(0,i)}(x, y, z)$$

we find that these mappings are conjugate to the mappings $\mathbf{T}^S_{(0,i)}(x', y', z')$ associated with the corresponding untransformed motion field $\mathbf{D}^S_{(0,i)}(x', y', z')$. The homomorphism that facilitates the conjugate relationship between the untransformed and transformed mappings is the transformation

$$\mathbf{F}_{(R,S)} : (x, y, z) \longmapsto (x'(x, y, z), y'(x, y, z), z'(x, y, z))$$

which defines the coordinate transformation between the reference and the subject. One interesting property of a pair of maps

that are conjugate to one another is the relationship between the fixed points of each. Consider a fixed point $x_0 \in X$. Then

$$
\begin{aligned}
x_0 &= g(x_0) \\
\Leftrightarrow x_0 &= F^{-1}(f(F(x_0))) \\
\Leftrightarrow F(x_0) &= f(F(x_0))
\end{aligned}
$$

and so the corresponding point $F(x_0) = x_0' \in X'$ is then a fixed point of f.

To see how the first order derivatives of conjugate mappings are related to each other we further assume for the sake of simplicity that $n = 1$, i.e., that conjugate maps f and g are scalar functions defined on the real line $\Re$, and that the conjugation is facilitated by the map F. Consider a point $x_0 \in X$. Then

$$
g(x_0) = F^{-1}(f(F(x_0))).
$$

By 2 applications of the chain rule

$$
g_x(x_0) = F_{x'}^{-1}(f(F(x_0)) f_{x'}(F(x_0)) F_x(x_0).
$$

The first element of the product can be evaluated using the chain rule

$$
F_{x'}^{-1}(f(F(x_0)) = \frac{1}{F_x(F^{-1}f F(x_0))}.
$$

Substituting this into the original expression gives

$$
\begin{aligned}
g_x(x_0) &= f_{x'}(F(x_0)) \frac{F_x(x_0)}{F_x(F^{-1}f F(x_0))} \\
&= f_{x'}(F(x_0)) \frac{F_x(x_0)}{F_x(g(x_0))}.
\end{aligned}
$$

Note that $f_{x'}(F(x_0))$ is the derivative of the original map f evaluated at the corresponding point $x_0' \in X'$ since $x_0' = F(x_0)$. This derivative has, therefore, been multiplied by a scaling factor

$$
\frac{F_x(x_0)}{F_x(g(x_0))}
$$

when producing the transformed conjugated map g.

We can extend this result to n-dimensional maps in the following way. Let $\boldsymbol{f}$ and $\boldsymbol{g}$ be n-dimensional maps facilitated by an n-dimensional map $\boldsymbol{F}$

$$
\begin{aligned}
\boldsymbol{f} &= (f^1(x_1, x_2, \ldots, x_n), \ldots, f^n(x_1, x_2, \ldots, x_n)) \\
\boldsymbol{g} &= (g^1(x_1, x_2, \ldots, x_n), \ldots, g^n(x_1, x_2, \ldots, x_n)) \\
\boldsymbol{F} &= (F^1(x_1, x_2, \ldots, x_n), \ldots, F^n(x_1, x_2, \ldots, x_n)).
\end{aligned}
$$

Once again consider a point $\boldsymbol{x_o} \in X$. Then, the Jacobian matrix of the conjugate map $\boldsymbol{g}$ can be calculated using the chain rule once again

$$
\begin{aligned}
\boldsymbol{g}(\boldsymbol{x_o}) &= F^{-1}(\boldsymbol{f}(\boldsymbol{F}(\boldsymbol{x_o}))) \\
g_{x_j}^i(\boldsymbol{x_o}) &= [F^{-1}]_{x_j'}^i(\boldsymbol{f}(\boldsymbol{F}(\boldsymbol{x_o}))) f_{x_j'}^i(\boldsymbol{F}(\boldsymbol{x_o})) F_{x_j}^i(\boldsymbol{x_o}).
\end{aligned}
$$

The first matrix in the product can be calculated using the chain rule

$$
[F^{-1}]_{x_j'}^i(\boldsymbol{f}(\boldsymbol{F}(\boldsymbol{x_o}))) = \left[F_{x_j}^i(\boldsymbol{F}^{-1}(\boldsymbol{f}(\boldsymbol{F}(\boldsymbol{x_o})))) \right]^{-1}.
$$

Substituting this into the original expression gives

$$
\begin{aligned}
g_{x_j}^i(\boldsymbol{x_o}) &= \left[F_{x_j}^i(\boldsymbol{F}^{-1}(\boldsymbol{f}(\boldsymbol{F}(\boldsymbol{x_o})))) \right]^{-1} f_{x_j'}^i(\boldsymbol{F}(\boldsymbol{x_o})) F_{x_j}^i(\boldsymbol{x_o}) \\
g_{x_j}^i(\boldsymbol{x_o}) &= \left[F_{x_j}^i(\boldsymbol{g}(\boldsymbol{x_o})) \right]^{-1} f_{x_j'}^i(\boldsymbol{F}(\boldsymbol{x_o})) F_{x_j}^i(\boldsymbol{x_o}).
\end{aligned}
$$

Taking determinants of both sides of the expression gives the following expression relating the volume changes of each function:

$$
\Phi_{\boldsymbol{g}}(\boldsymbol{x_o}) = \Phi_{\boldsymbol{f}}(\boldsymbol{F}(\boldsymbol{x_o})) \frac{\Phi_{\boldsymbol{F}}(\boldsymbol{x_o})}{\Phi_{\boldsymbol{F}}(\boldsymbol{g}(\boldsymbol{x_o}))}.
$$

Once again, $\Phi_{\boldsymbol{f}}(\boldsymbol{F}(\boldsymbol{x_o})$ is the volume-change function of the original mapping $\boldsymbol{f}$ evaluated at the corresponding point $\boldsymbol{x_o'} \in X'$ because $\boldsymbol{x_o'} = F(\boldsymbol{x_o})$. We can see that the volume change has been multiplied by the scaling factor

$$
\frac{\Phi_{\boldsymbol{F}}(\boldsymbol{x_o})}{\Phi_{\boldsymbol{F}}(\boldsymbol{g}(\boldsymbol{x_o}))}
$$

when producing the transformed conjugated map $\boldsymbol{g}$. Applying this result to the volume-change images we produced in Section III-D, we can see why Fig. 8(a) and (b) are not identical. Adopting the approach used to produce a volume-change image such as that shown in Fig. 8(a), the image would be defined as

$$
\Phi(\boldsymbol{x_o}) = \Phi_{\boldsymbol{f}}(\boldsymbol{F}(\boldsymbol{x_o}))
$$

where the volume-change at the point $\boldsymbol{x_o}$ is equal to the volume change at the corresponding point $\boldsymbol{F}(\boldsymbol{x_o})$. In Fig. 8(b), on the other hand, the volume-change image would be equal to

$$
\Phi(\boldsymbol{x_o}) = \Phi_{\boldsymbol{f}}(\boldsymbol{F}(\boldsymbol{x_o})) \frac{\Phi_{\boldsymbol{F}}(\boldsymbol{x_o})}{\Phi_{\boldsymbol{F}}(\boldsymbol{g}(\boldsymbol{x_o}))}.
$$

Clearly, if $\Phi_{\boldsymbol{F}}(\boldsymbol{x_o}) = \Phi_{\boldsymbol{F}}(\boldsymbol{g}(\boldsymbol{x_o}))$ then the scaling factor is equal to 1 at $\boldsymbol{x_o}$ and so the volume-change functions are the same using either of the two approaches. There are two obvious ways of this happening. First, if $\boldsymbol{x_o} = \boldsymbol{g}(\boldsymbol{x_o})$, i.e., $\boldsymbol{x_o}$ is a fixed point of $\boldsymbol{g}$, then the scaling factor is equal to 1 at the fixed point and so the volume change functions are the same using either of the two approaches. By continuity, we would also expect the volume-change functions to be very similar to each other at $\boldsymbol{x_o}$ if $\boldsymbol{x_o} \approx \boldsymbol{g}(\boldsymbol{x_o})$, i.e., if the deformations associated with the conjugate map are small. Second, we can see that the scaling factor will be 1 everywhere if $\Phi_{\boldsymbol{F}}$ is constant since then $\Phi_{\boldsymbol{F}}(\boldsymbol{x_o}) = \Phi_{\boldsymbol{F}}(\boldsymbol{g}(\boldsymbol{x_o}))$ for all $\boldsymbol{x_o}$. Such a situation would arise if $\boldsymbol{F}$ is an n-dimensional affine map, which in the case that $n = 3$ would mean that $\boldsymbol{F}$ is a mapping encompassing a rigid body rotation and anisotropic scaling and skewing. By continuity, we would also expect the volume-change functions

to be very similar to each other at x_o if the first order derivatives of F do not change much between x_o and $g(x_o)$.

One further point of interest is that the qualitative nature of the deformations in a local neighborhood of a fixed point, x_o of g are the same as the qualitative nature of the deformations in a local neighborhood of the corresponding fixed point $F(x_o)$ of f. The reason is that the matrix expression

$$g_{x_j}^i(x_o) = \left[F_{x_j}^i(g(x_o)) \right]^{-1} f_{x'_j}^i(F(x_o)) F_{x_j}^i(x_o)$$

reduces to

$$g_{x_j}^i(x_o) = \left[F_{x_j}^i(x_o) \right]^{-1} f_{x'_j}^i(F(x_o)) F_{x_j}^i(x_o)$$

if x_o is a fixed point of g, in which case $F_{x_j}^i(x_o)$ acts as a "change of basis" matrix on $f_{x'_j}^i(F(x_o))$. This means that $g_{x_j}^i(x_o)$ is a "similar" matrix to $f_{x'_j}^i(F(x_o))$, and that the local phase portrait behavior is qualitatively identical for both f and g at corresponding fixed points.

REFERENCES

[1] A. Janke, G. de Zubicaray, S. Rose, M. Griffin, J. Chalk, and G. Galloway, "4D deformation modeling of cortical disease progression in Alzheimer's dementia," *Magn. Reson. Med.*, vol. 46, no. 4, pp. 661–666, 2001.

[2] W. Crum, R. Scahill, and N. Fox, "Automated hippocampal segmentation by regional fluid registration of serial MRI," *Neuroimage*, vol. 13, no. 5, pp. 847–855, 2001.

[3] P. Freeborough and N. Fox, "Modeling brain deformations in alzheimer disease by fluid registration of serial 3D MR images," *J. Comput. Assist. Tomogr.*, vol. 22, no. 5, pp. 838–843, 1998.

[4] P. Thompson, J. Giedd, R. P. Woods, D. Macdonald, A. Evans, and A. Toga, "Growth patterns in the developing brain detected using continuum mechanical tensor maps," *Nature*, vol. 404, pp. 190–193, 2003.

[5] R. Chandrashekara, R. H. Mohiaddin, and D. Rueckert, "Analysis of myocardial motion in tagged MR images using nonrigid image registration," in *Proc. SPIE Int. Symp. Medical Imaging*, M. Sonka and J. M. Fitzpatrick, Eds., San Diego, CA, 2002, pp. 1168–1179.

[6] E. A. Zerhouni, D. M. Parish, W. J. Rogers, A. Yang, and E. P. Shapiro, "Human heart: Tagging with MR imaging—A method for noninvasive assessment of myocardial motion," *Radiology*, vol. 169, no. 1, pp. 59–63, 1988.

[7] L. Axel and L. Dougherty, "MR imaging of motion with spatial modulation of magnetization," *Radiology*, vol. 171, no. 3, pp. 841–845, 1989.

[8] L. Dougherty, J. J. Pilla, A. S. Bloom, S. V. Pusca, and M. A. Acker, "3D multiphase MR tagged imaging of canine cardiomyoplasty," in *Proc. IEEE 25th Annu. Northeast Bioengineering Conf.*, M. Nowak, R. Adrezin, and D. Leone, Eds., 1999, pp. 83–84.

[9] S. N. Gupta and J. L. Prince, "On variable brightness optical flow for tagged MRI," in *Proc. 15th Int. Conf. Information Processing in Medical Imaging (IPMI)*, June 1995, pp. 323–334.

[10] A. A. Amini, Y. Chen, R. W. Curwen, V. Mani, and J. Sun, "Coupled B-snake grids and constrained thin-plate splines for analysis of 2-D tissue deformations from tagged MRI," *IEEE Trans. Med. Imag.*, vol. 17, pp. 344–356, June 1998.

[11] A. A. Amini, Y. Chen, M. Elayyadi, and P. Radeva, "Tag surface reconstruction and tracking of myocardial beads from SPAMM-MRI with parametric B-spline surfaces," *IEEE Trans. Med. Imag.*, vol. 20, pp. 94–103, Feb. 2001.

[12] M. A. Guttman, J. L. Prince, and E. R. McVeigh, "Tag and contour detection in tagged MR images of the left ventricle," *IEEE Trans. Med. Imeg.*, vol. 13, Mar. 1994.

[13] J. Huang, D. Abendschein, V. G. Dávila-Román, and A. A. Amini, "Spatio-temporal tracking of myocardial deformations with a 4-D B-spline model from tagged MRI," *IEEE Trans. Med. Imag.*, vol. 18, pp. 957–972, Oct. 1999.

[14] S. Kumar and D. Goldgof, "Automatic tracking of SPAMM grid and the estimation of deformation parameters from cardiac MR images," *IEEE Trans. Med. Imag.*, vol. 13, pp. 122–132, Mar. 1994.

[15] J. Park, D. Metaxas, and L. Axel, "Analysis of left ventricular wall motion based on volumetric deformable models and MRI-SPAMM," *Med. Image Anal.*, vol. 1, no. 1, pp. 53–71, 1996.

[16] J. Park, D. Metaxas, A. A. Young, and L. Axel, "Deformable models with parameter functions for cardiac motion analysis from tagged MRI data," *IEEE Trans. Med. Imag.*, vol. 15, pp. 278–289, June 1996.

[17] P. Radeva, A. A. Amini, and J. Huang, "Deformable B-solids and implicit snakes for 3D localization and tracking of SPAMM MRI data," *Comput. Vis. Image Understanding*, vol. 66, no. 2, pp. 163–178, May 1997.

[18] D. Alexander and J. Gee, "Spatial transformations for registration of dt-mris," in *Proc. Medical Image Understanding and Analysis Conf.*, London, U.K., 2000, pp. 203–206.

[19] D. Alexander, C. Pierpaoli, P. Basser, and J. Gee, "Spatial transformations of diffusion tensor magnetic resonance images," *IEEE Trans. Med. Imag.*, vol. 20, pp. 1131–1139, Nov. 2001.

[20] D. Xu, S. Mori, D. Shen, P. van Zijl, and C. Davatzikos, "Spatial normalization of diffusion tensor fields," *Magn. Reson. Med.*, vol. 50, no. 1, pp. 175–182, 2003.

[21] H. J. Johnson and G. E. Christensen, "Consistent landmark and intensity-based image registration," *IEEE Trans. Med. Imag.*, vol. 21, pp. 450–461, May 2002.

[22] A. Rao, G. I. Sanchez-Ortiz, R. Chandrashekara, M. Lorenzo-Valdes, R. Mohiaddin, and D. Rueckert, "Comparison of cardiac motion across subjects using nonrigid registration," in *Lecture Notes in Computer Science*, T. Dohi and R. Kikinis, Eds. Berlin, Germany, 2002, vol. 2489, Fifth Int. Conf. on Medical Image Computing and Computer-Assisted Intervention (MICCAI '02), pp. 722–729.

[23] ——, "Construction of a cardiac motion atlas from MR using nonrigid registration," in *Lecture Notes in Computer Science*, I. Magnin, J. Montagnat, P. Clarysse, J. Neonen, and T. Katila, Eds. Lyons, France, 2003, vol. 2674, Second International Workshop on Functional Imaging and Modeling of the Heart, pp. 141–150.

[24] D. Rueckert, L. I. Sonoda, C. Hayes, D. L. G. Hill, M. O. Leach, and D. J. Hawkes, "Nonrigid registration using free-form deformations: Application to breast MR images," *IEEE Trans. Med. Imag.*, vol. 18, pp. 712–721, Aug. 1999.

[25] C. Studholme, D. L. G. Hill, and D. J. Hawkes, "An overlap invariant entropy measure of 3D medical image alignment," *Pattern Recognit.*, vol. 32, no. 1, pp. 71–86, 1999.

[26] P. J. Edwards, D. L. G. Hill, J. A. Little, and D. J. Hawkes, "A three-component deformation model for image-guided surgery," *Med. Image Anal.*, vol. 2, no. 4, pp. 355–367, 1998.

[27] J. A. Schnabel, D. Rueckert, M. Quist, J. M. Blackall, A. D. C. Smith, T. Hartkens, G. P. Penney, W. A. Hall, H. Liu, C. L. Truwit, F. A. Gerritsen, D. L. G. Hill, and D. J. Hawkes, "A generic framework for nonrigid registration based on nonuniform multi-level free-form deformations," in *Lecture Notes in Computer Science*, W. Niessen and M. Viergever, Eds. Berlin, Germany: Springer-Verlag, Oct. 2001, vol. 2208, 4th Int. Conf. Medical Image Computing and Computer-Assisted Intervention (MICCAI '01), pp. 573–581.

[28] R. Chandrashekara, A. Rao, G. I. Sanchez-Ortiz, R. H. Mohiaddin, and D. Rueckert, "Construction of a statistical model for cardiac motion analysis using nonrigid image registration," in *Lecture Notes in Computer Science*, C. Taylor and J. A. Noble, Eds. Berlin, Germany: Springer-Verlag, 2003, 18th Int. Conf. on Information Processing in Medical Imaging (IPMI), pp. 599–610.

[29] B. K. Puri, N. Saeed, A. Oatridge, J. V. Hajnal, S. B. Hutton, L. J. Duncan, M. J. Chapman, T. R. E. B. TRE, G. M. Bydder, and E. M. Joyce, "A longitudinal MRI study of first-episode schizophrenia: Assessment of cerebral changes and quantitation of ventricular change," *Schizophrenia Res.*, vol. 29, no. 1–2, pp. 76–77, 1998.

[30] D. L. Collins, A. P. Zijdenbos, V. Kollokian, J. G. Sled, N. J. Kabani, C. J. Holmes, and A. C. Evans, "Design and construction of a realistic digital brain phantom," *IEEE Trans. Med. Imag.*, vol. 17, pp. 463–468, June 1998.